IET Microwaves, Antennas & Propagation

Research Article

Quasi-trapezoidal microstrip spherical patches and arrays

ISSN 1751-8725
Received on 27th February 2015
Revised on 20th August 2015
Accepted on 2nd September 2015
doi: 10.1049/iet-map.2015.0145
www.ietdl.org

Leonardo A. Costa[1], *Odilon Maroja da Costa Pereira-Filho*[2] ✉, *Fernando J.S. Moreira*[3]

[1]*PETROBRAS, Rio de Janeiro, Brazil*
[2]*Informatics Center, Federal University of Pernambuco, Recife, Brazil*
[3]*Department of Electronics Engineering, Federal University of Minas Gerais, Belo Horizonte, Brazil*
✉ *E-mail: odilon@cin.ufpe.br*

Abstract: This study presents a full-wave analysis of quasi-trapezoidal microstrip spherical patches and arrays. It uses method of moments to evaluate the effect of the shape of the patches on the input impedance, bandwidth, mutual impedance, and radiation pattern. Arrays of quasi-trapezoidal patches are also analysed. Presents a procedure for avoiding numerical problems on evaluating combinations of Schelkunoff Bessel functions. Results are compared with previously published ones for the quasi-rectangular case for validation.

1 Introduction

Microstrip antennas have been widely used due to some of their characteristics, as light weight, low profile, and how easily they conform to surfaces. Reviews of non-planar microstrip antennas are presented at [1–3]. Spherical microstrip antennas find important applications in aeronautics and satellite communications. Such antennas have been studied using several techniques, including cavity method [4–9], electric surface current method [10], generalised transmission line model [11, 12], and method of moments (MoM) [13–20].

MoM was initially employed in [13] for determining the resonances of a circular microstrip disk mounted on a spherical surface, or in the presence of a superstrate [14]. While input impedance of spherical circular and annular microstrip antennas were shown in [15]. Quasi-rectangular spherical microstrip patches and arrays were presented in [16–19], using MoM. These formulations used full-domain basis functions, with no transversal variation of the currents. In [20] the patch was no longer limited to a quasi-rectangular shape, and the input impedance was obtained from moment method and attachment modes. Antenna analyses in multilayered spherical media are presented in [21–25]. Curvilinear Rao–Wilton–Glisson triangular basis functions were also used in [26, 27] for modelling antennas in spherical layered media.

This work intends to analyse arrays of spherical patches of quasi-trapezoidal shape, as shown in Fig. 1, and to observe the effects of the shape on the antenna characteristics. This patch shapes adjust naturally into spherical geometries, and are alternative to rectangular ones. The paper also introduces a numerical procedure for evaluation of combinations of Schelkunoff Bessel functions that avoids computational limitations, allowing an accurate evaluation of the MoM matrix elements, that could be used for larger problems. The array analysis takes the coupling among the elements into consideration.

2 MoM solution

The geometry of the spherical patches is shown in Fig. 1. A spherical perfect conductor of radius r_1, is covered by a dielectric layer of thickness h ($r_2 = r_1 + h$), dielectric constant ε_r, and loss tangent $\tan\delta$. There is a total of N_p spherical patches (only two are visible in Fig. 1) printed over the dielectric surface $r = r_2$, limited by angles θ_1 and θ_2 [mean $\theta_c = (\theta_1 + \theta_2)/2$]. The patch i ranges from $\phi_1(i)$ to $\phi_2(i)$, $i = 1, \ldots, N_p$. The width of the patches in θ-direction values $W_\theta = r_2\Delta_\theta$, where $\Delta_\theta = \theta_2 - \theta_1$. The widths of the patches in ϕ-direction vary from θ_1 to θ_2, and a mean width of the patch i, measured at $\theta = \theta_c$, values $W_\phi(i) = r_2 \sin(\theta_c)\Delta_\phi(i)$, where $\Delta_\phi(i) = \phi_2(i) - \phi_1(i)$.

The analysis uses the vector Legendre series [10] in its normalised form [16], as presented in Appendix, along with the definition of the normalised associated Legendre functions $\bar{P}_n^m(.)$. The problem is formulated using MoM [28], as described next.

2.1 Green's functions

Although the Green's functions are unique and can be found in previous works [10, 13, 14], they are written below in a special a way to avoid numerical problems from combinations of the Schelkunoff Bessel functions. The Green's function for the tangential electric field (θ and ϕ components) due to an electric dipole printed over the dielectric layer ($r = r_2$), in spectral domain, can be written as

$$\overline{\overline{G_t^{\mathrm{Ed}}}}(r, n) = \begin{bmatrix} G_{11}^{\mathrm{Ed}}(r, n) & 0 \\ 0 & G_{22}^{\mathrm{Ed}}(r, n) \end{bmatrix} \tag{1}$$

$$\overline{\overline{G_t^{\mathrm{Eo}}}}(r, n) = \begin{bmatrix} G_{11}^{\mathrm{Eo}}(r, n) & 0 \\ 0 & G_{22}^{\mathrm{Eo}}(r, n) \end{bmatrix} \tag{2}$$

where

$$G_{11}^{\mathrm{Ed}}(r,n) = -j\frac{r_2}{r}\frac{D_1(n,r_1,r)}{D_1(n,r_1,r_2)}\left(\frac{1}{\eta_o}\frac{\hat{H}_n^{(2)}(k_o r_2)}{\hat{H}_n^{(2)'}(k_o r_2)} - \frac{1}{\eta_d}\frac{D_3(n,r_1,r_2)}{D_1(n,r_1,r_2)}\right)^{-1} \tag{3}$$

$$G_{22}^{\mathrm{Ed}}(r,n) = -j\frac{r_2}{r}\frac{D_5(n,r_1,r)}{D_5(n,r_1,r_2)}\left(-\frac{1}{\eta_o}\frac{\hat{H}_n^{(2)'}(k_o r_2)}{\hat{H}_n^{(2)}(k_o r_2)} + \frac{1}{\eta_d}\frac{D_7(n,r_1,r_2)}{D_5(n,r_1,r_2)}\right)^{-1} \tag{4}$$

$$G_{11}^{\mathrm{Eo}}(r,n) = -j\frac{r_2}{r}\frac{\hat{H}_n^{(2)'}(k_o r)}{\hat{H}_n^{(2)'}(k_o r_2)}\left(\frac{1}{\eta_o}\frac{\hat{H}_n^{(2)}(k_o r_2)}{\hat{H}_n^{(2)'}(k_o r_2)} - \frac{1}{\eta_d}\frac{D_3(n,r_1,r_2)}{D_1(n,r_1,r_2)}\right)^{-1} \tag{5}$$

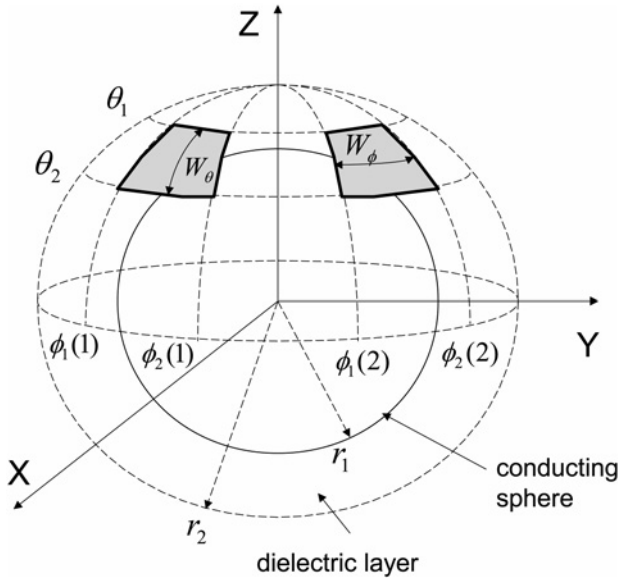

Fig. 1 *Geometry of the spherical microstrip patches*

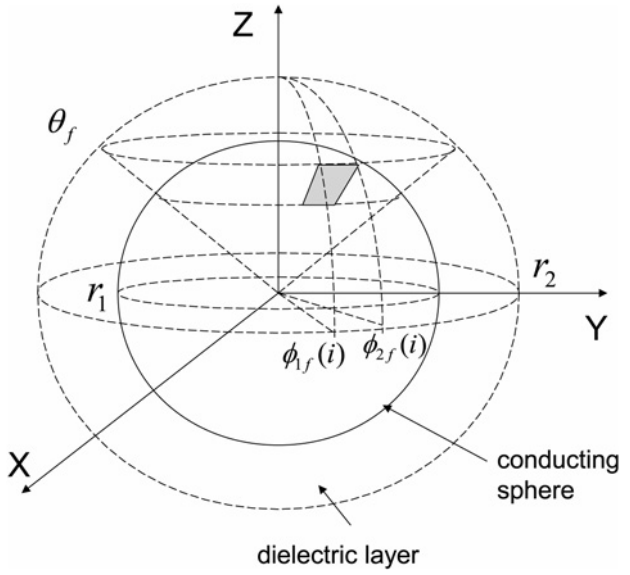

Fig. 2 *Details of the feeding strip for patch i*

$$G_{22}^{\mathrm{Eo}}(r,n) = -j\frac{r_2}{r}\frac{\hat{H}_n^{(2)}(k_\mathrm{o}r)}{\hat{H}_n^{(2)}(k_\mathrm{o}r_2)}\left(-\frac{1}{\eta_\mathrm{o}}\frac{\hat{H}_n^{(2)'}(k_\mathrm{o}r_2)}{\hat{H}_n^{(2)}(k_\mathrm{o}r_2)}+\frac{1}{\eta_\mathrm{d}}\frac{D_7(n,r_1,r_2)}{D_5(n,r_1,r_2)}\right)^{-1} \tag{6}$$

and

$$D_1(n,r_1,r) = \hat{N}_n'(k_\mathrm{d}r_1)\hat{J}_n'(k_\mathrm{d}r) - \hat{J}_n'(k_\mathrm{d}r_1)\hat{N}_n'(k_\mathrm{d}r) \tag{7}$$

$$D_3(n,r_1,r) = \hat{N}_n'(k_\mathrm{d}r_1)\hat{J}_n(k_\mathrm{d}r) - \hat{J}_n'(k_\mathrm{d}r_1)\hat{N}_n(k_\mathrm{d}r) \tag{8}$$

$$D_5(n,r_1,r) = \hat{N}_n(k_\mathrm{d}r_1)\hat{J}_n(k_\mathrm{d}r) - \hat{J}_n(k_\mathrm{d}r_1)\hat{N}_n(k_\mathrm{d}r) \tag{9}$$

$$D_7(n,r_1,r) = \hat{N}_n(k_\mathrm{d}r_1)\hat{J}_n'(k_\mathrm{d}r) - \hat{J}_n(k_\mathrm{d}r_1)\hat{N}_n'(k_\mathrm{d}r) \tag{10}$$

$\overline{\overline{G_t^{\mathrm{Eo}}}}$ and $\overline{\overline{G_t^{\mathrm{Ed}}}}$ are the Green's functions in the air ($r \geq r_2$) and in the dielectric ($r_1 \leq r \leq r_2$), respectively, η_o and η_d are the intrinsic impedances of air and dielectric, respectively, k_o and k_d are the wavenumbers of air and dielectric, respectively, and $\hat{B}_n(.)$ represents the Schelkunoff Bessel functions in usual notation [29]. The tangential electric field in each region (dielectric and air), in spectral domain, due to a surface current distribution $\bar{J}(\theta, \phi)$ is obtained from the Green's functions by

$$\tilde{E}_t^{\mathrm{o}}(r,n,m) = \overline{\overline{G_t^{\mathrm{Eo}}}}(r,n)\tilde{J}(n,m) \tag{11}$$

$$\tilde{E}_t^{\mathrm{d}}(r,n,m) = \overline{\overline{G_t^{\mathrm{Ed}}}}(r,n)\tilde{J}(n,m) \tag{12}$$

where $\tilde{J}(n,m)$ is the normalised vector Legendre transform of $\bar{J}(\theta, \phi)$. At the surface $r = r_2$ the Green's function is explicitly given by

$$\overline{\overline{G_t^{\mathrm{Eo}}}}(r_2,n) = \begin{bmatrix} G_{11}^{\mathrm{E}}(n) & 0 \\ 0 & G_{22}^{\mathrm{E}}(n) \end{bmatrix} \tag{13}$$

where

$$G_{11}^{\mathrm{E}}(n) = -j\left(\frac{1}{\eta_\mathrm{o}}\frac{\hat{H}_n^{(2)}(k_\mathrm{o}r_2)}{\hat{H}_n^{(2)'}(k_\mathrm{o}r_2)} - \frac{1}{\eta_\mathrm{d}}\frac{D_3(n,r_1,r_2)}{D_1(n,r_1,r_2)}\right)^{-1} \tag{14}$$

$$G_{22}^{\mathrm{E}}(n) = -j\left(-\frac{1}{\eta_\mathrm{o}}\frac{\hat{H}_n^{(2)'}(k_\mathrm{o}r_2)}{\hat{H}_n^{(2)}(k_\mathrm{o}r_2)}+\frac{1}{\eta_\mathrm{d}}\frac{D_7(n,r_1,r_2)}{D_5(n,r_1,r_2)}\right)^{-1} \tag{15}$$

2.2 Excitation

The patches are fed by coaxial cables. To simplify the MoM procedure, the probes are modelled by equivalent strips, as shown in Fig. 2, of width equal to 5 times de diameter of the probe [30]. This is a usual model for the probe, and an alternative for the model as filament of zero diameter. Consider the patch i ($i = 1, \ldots, N_p$). The equivalent strip is placed at $\theta = \theta_f$, limited by the angles $\phi_{1f}(i)$ and $\phi_{2f}(i)$, from $r = r_1$ to $r = r_2$. It should be noted that the width of the strip [$= r\sin(\theta_f)\Delta_{\phi f}(i)$, where $\Delta_{\phi f}(i) = \phi_{2f}(i) - \phi_{1f}(i)$] varies with the radius r. A mean width of the strip i is defined haft way into the dielectric as $W_{fi} = r_{12}\sin(\theta_f)\Delta_{\phi f}(i)$, where $r_{12} = (r_1 + r_2)/2$. In fact the dielectric thickness h is normally small, resulting in an equivalent strip of almost constant width. The r-directed volume current distribution on feed i is given by

$$J_{fi}(r,\theta,\phi) = \frac{I_\mathrm{o}(i)}{r^2\sin(\theta_f)\Delta_{\phi f}(i)}\delta(\theta-\theta_f), \quad r_1 < r < r_2, \quad \phi_{1f}(i) < \phi < \phi_{2f}(i) \tag{16}$$

It corresponds to a total current $I_\mathrm{o}(i)$ at each patch feeder. Using the Fourier–Legendre series

$$J_{fi}(r,\theta,\phi) = \sum_{m=-\infty}^{\infty}\sum_{n=|m|}^{\infty}\tilde{J}_{fi}(r,n,m)\bar{P}_n^{|m|}(\cos\theta)\,\mathrm{e}^{\mathrm{j}m\phi} \tag{17}$$

$$\tilde{J}_{fi}(r,n,m) = \frac{2n+1}{4\pi}\int_0^{\pi}\int_{-\pi}^{\pi}J_{fi}(r,\theta,\phi)\bar{P}_n^{|m|}x(\cos\theta)\,\mathrm{e}^{-\mathrm{j}m\phi}\sin\theta\,\mathrm{d}\theta\,\mathrm{d}\phi \tag{18}$$

The transform of $J_{fi}(r, \theta, \phi)$ is given by

$$\tilde{J}_{fi}(r,n,m) = \frac{2n+1}{4\pi}\frac{I_\mathrm{o}(i)}{r^2}\bar{P}_n^{|m|}(\cos(\theta_f))\,\mathrm{e}^{-\mathrm{j}m\phi_f(i)}\mathrm{sinc}\left(\frac{m\Delta_{\phi f}(i)}{2\pi}\right) \tag{19}$$

where $\phi_f(i) = (\phi_{1f}(i) + \phi_{2f}(i))/2$ and $\mathrm{sinc}(x) = \sin(\pi x)/(\pi x)$. An array

IET Microw. Antennas Propag., 2016, Vol. 10, Iss. 1, pp. 53–60

of N_p spherical patches is fed by a network of N_p probes, with currents $J_{fi}(r, \theta, \phi)$.

2.3 Full-domain basis functions

The currents on the spherical patches are expanded into a set of full-domain basis, as follows

$$J_\theta(\theta, \phi) = \sum_{i=1}^{N_p} \sum_{q=1}^{Q_\theta} \sum_{p=0}^{P_\theta} a_{iqp} J_{\theta iqp}(\theta, \phi) \tag{20}$$

$$J_\phi(\theta, \phi) = \sum_{i=1}^{N_p} \sum_{q=0}^{Q_\phi} \sum_{p=1}^{P_\phi} b_{iqp} J_{\phi iqp}(\theta, \phi) \tag{21}$$

where a_{iqp} and b_{iqp} are the coefficients to be determined. The θ-directed basis functions are given by

$$J_{\theta iqp}(\theta, \phi) = f_{\theta q}(\theta) g_{\theta ip}(\phi) \tag{22}$$

where

$$f_{\theta q}(\theta) = \frac{\sin\big((q\pi/\Delta_\theta)(\theta - \theta_1)\big)}{\sin\theta} \tag{23}$$

$$g_{\theta ip}(\phi) = \cos\left(\frac{p\pi}{\Delta_\phi(i)}(\phi - \phi_1(i))\right) \tag{24}$$

and its normalised vector Legendre transform (67) values

$$\tilde{J}_{\theta iqp}(n, m) = \frac{1}{\sqrt{S(n)}} \begin{bmatrix} F_\theta^{(2)}(n, m, q) G_\theta(m, i, p) \\ \mathrm{j}m F_\theta^{(1)}(n, m, q) G_\theta(m, i, p) \end{bmatrix} \tag{25}$$

where

$$F_\theta^{(1)}(n, m, q) = \int_0^\pi f_{\theta q}(\theta) \bar{P}_n^{|m|}(\cos\theta)\, \mathrm{d}\theta \tag{26}$$

$$F_\theta^{(2)}(n, m, q) = \int_0^\pi f_{\theta q}(\theta) \frac{\partial}{\partial\theta} \bar{P}_n^{|m|}(\cos\theta) \sin\theta\, \mathrm{d}\theta \tag{27}$$

$$G_\theta(m, i, p) = \int_{-\pi}^{\pi} g_{\theta ip}(\phi)\, \mathrm{e}^{-\mathrm{j}m\phi}\, \mathrm{d}\phi \tag{28}$$

The ϕ-directed basis functions are given by

$$J_{\phi iqp}(\theta, \phi) = f_{\phi q}(\theta) g_{\phi ip}(\phi) \tag{29}$$

where

$$f_{\phi q}(\theta) = \cos\left(\frac{q\pi}{\Delta_\theta}(\theta - \theta_1)\right) \tag{30}$$

$$g_{\phi ip}(\phi) = \sin\left(\frac{p\pi}{\Delta_\phi(i)}(\phi - \phi_1(i))\right) \tag{31}$$

and its normalised vector Legendre transform values

$$\tilde{J}_{\phi iqp}(n, m) = \frac{1}{\sqrt{S(n)}} \begin{bmatrix} -\mathrm{j}m F_\phi^{(1)}(n, m, q) G_\phi(m, i, p) \\ F_\phi^{(2)}(n, m, q) G_\phi(m, i, p) \end{bmatrix} \tag{32}$$

where

$$F_\phi^{(1)}(n, m, q) = \int_0^\pi f_{\phi q}(\theta) \bar{P}_n^{|m|}(\cos\theta)\, \mathrm{d}\theta \tag{33}$$

$$F_\phi^{(2)}(n, m, q) = \int_0^\pi f_{\phi q}(\theta) \frac{\partial}{\partial\theta} \bar{P}_n^{|m|}(\cos\theta) \sin\theta\, \mathrm{d}\theta \tag{34}$$

$$G_\phi(m, i, p) = \int_{-\pi}^{\pi} g_{\phi ip}(\phi)\, \mathrm{e}^{-\mathrm{j}m\phi}\, \mathrm{d}\phi \tag{35}$$

The integrals $F_\theta^{(1)}(n, m, q)$, $F_\theta^{(2)}(n, m, q)$, $F_\phi^{(1)}(n, m, q)$, and $F_\phi^{(2)}(n, m, q)$ are numerically evaluated just once, as they are frequency independent. $G_\theta(m, i, p)$ and $G_\phi(m, i, p)$ on the other hand, can be easily obtained analytically. Full-domain basis functions used allow transversal variation of the currents, although they did not result in improvements of input impedance.

2.4 MoM linear system

The MoM linear system is formed by imposing the boundary conditions on the patch surfaces and taking the symmetric product by a set of testing functions, which are chosen the same as the basis functions, resulting in a Galerkin method. The procedure is well known and will be presented in summarised form. The symmetric product is defined as

$$\langle f, g \rangle_s = \int_0^\pi \int_{-\pi}^{\pi} f(\theta, \phi) g(\theta, \phi) r_2^2 \sin\theta\, \mathrm{d}\theta \tag{36}$$

The resulting linear system ($[Z][I] = [V]$) can be written as

$$\begin{bmatrix} [\boldsymbol{Z}^{\theta\theta}] & [\boldsymbol{Z}^{\theta\phi}] \\ [\boldsymbol{Z}^{\phi\theta}] & [\boldsymbol{Z}^{\phi\phi}] \end{bmatrix} \begin{bmatrix} [a] \\ [b] \end{bmatrix} = \begin{bmatrix} [V^\theta] \\ [V^\phi] \end{bmatrix} \tag{37}$$

where each element of the matrix $[\boldsymbol{Z}]$ is of the following form

$$\begin{aligned} Z_{\text{test,basis}} &= \langle \bar{E}(\bar{J}_{\text{basis}}), \bar{J}_{\text{test}} \rangle_s \\ &= r_2^2 \sum_{m=-\infty}^{\infty} \sum_{n=|m|}^{\infty} \big[\tilde{J}_{\text{test}}(n, -m)\big]^t \overline{\overline{G_t^{\text{Eo}}}}(r_2, n) \big[\tilde{J}_{\text{basis}}(n, m)\big] \end{aligned} \tag{38}$$

This general expression equals the elements of the submatrices $[\boldsymbol{Z}^{\theta\theta}]$, $[\boldsymbol{Z}^{\theta\phi}]$, $[\boldsymbol{Z}^{\phi\theta}]$ or $[\boldsymbol{Z}^{\phi\phi}]$, depending on the directions of the testing and basis functions. In (37) $[\boldsymbol{a}]$ and $[\boldsymbol{b}]$ are column matrices with the unknown coefficients. The elements of the matrix $[\boldsymbol{V}]$, with the aid of reciprocity theorem, can be obtained from

$$\begin{aligned} V_{\text{test}} &= -\langle \bar{E}(J_f), \bar{J}_{\text{test}} \rangle_s \\ &= -\frac{r_2}{\mathrm{j}w\varepsilon_d} \sum_{m=-\infty}^{\infty} \sum_{n=|m|}^{\infty} \frac{\sqrt{S(n)} J_u(n, m)}{D_1(n, r_1, r_2)} \\ &\quad \times \left(\frac{\eta_\mathrm{d}}{\eta_\mathrm{o}} \frac{\hat{H}_n^{(2)}(k_\mathrm{o} r_2)}{\hat{H}_n^{(2)'}(k_\mathrm{o} r_2)} - \frac{D_3(n, r_1, r_2)}{D_1(n, r_1, r_2)}\right)^{-1} \\ &\quad \times \int_{r_1}^{r_2} D_3(n, r_1, r) \bar{J}_f(r, n, -m)\, \mathrm{d}r \end{aligned} \tag{39}$$

where V_{test} reduces to the elements of V^θ or V^ϕ depending on the direction of the testing functions. In (39) $J_u(n, m)$ is the upper value of the transform of $\bar{J}_{\text{test}}$ [see (67)]. For $J_{\theta iqp}$ it can be obtained from (25) and for $J_{\phi iqp}$ from (32). J_f includes the feeding

currents of all patches excited:

$$J_f(r,\,\theta,\,\phi)=\sum_i J_{fi}(r,\,\theta,\,\phi) \tag{40}$$

The MoM linear system is solved for the coefficients a_{iqp} and b_{iqp}, completing the determination of the currents on the patches.

This formulation could be extended to multilayer patch antennas by altering the Green's functions; or to non-contact feeding, by including current modelling at the aperture or transmission line.

3 Numerical procedure

Numerical issues of the analysis are related to the evaluation of Schelkunoff Bessel functions in the Green's functions. The procedure proposed here starts from writing the Green's function in an appropriate form, as in (13)–(15), where the Schelkunoff Bessel functions appear in combinations as in (7)–(10), or as ratios $\hat{H}_n^{(2)}(x)/\hat{H}_n^{(2)'}(x)$. These combinations are evaluated differently according to the argument range, as follows:

(i) For very small arguments analytical limits of the Schelkunoff Bessel functions are used for computing the combinations. From [29] the functions and their derivatives tend to

$$\lim_{|z|\to 0}\hat{J}_n(z)=\frac{\sqrt{\pi}}{(n+1/2)!}\left(\frac{z}{2}\right)^{n+1} \tag{41}$$

$$\lim_{|z|\to 0}\hat{J}_n'(z)=\frac{\sqrt{\pi}}{(n+1/2)!}\frac{n+1}{2}\left(\frac{z}{2}\right)^{n} \tag{42}$$

$$\lim_{|z|\to 0}\hat{N}_n(z)=-\frac{(n-1/2)!}{\sqrt{\pi}}\left(\frac{2}{z}\right)^{n} \tag{43}$$

$$\lim_{|z|\to 0}\hat{N}_n'(z)=\begin{cases} z, & n=0 \\ \dfrac{n(n-1/2)!}{2\sqrt{\pi}}\left(\dfrac{2}{z}\right)^{n+1}, & n\neq 0 \end{cases} \tag{44}$$

Substituting (41)–(44) into (7)–(10)

$$\lim_{|k_o r_1|\to 0} D_1(n,\,r_1,\,r) = \begin{cases} k_d(r_1-r), & -n=0 \\ \dfrac{n(n+1)}{(2n+1)k_d}\left[\dfrac{1}{r_1}\left(\dfrac{r}{r_1}\right)^n-\dfrac{1}{r}\left(\dfrac{r_1}{r}\right)^n\right], & n\neq 0 \end{cases} \tag{45}$$

$$\lim_{|k_o r_1|\to 0} D_3(n,\,r_1,\,r) = \begin{cases} 1+k_d^2 r_1 r, & n=0 \\ \dfrac{n}{2n+1}\left(\dfrac{r}{r_1}\right)^{n+1}+\dfrac{n+1}{2n+1}\left(\dfrac{r_1}{r}\right)^n, & n\neq 0 \end{cases} \tag{46}$$

$$\lim_{|k_o r_1|\to 0} D_5(n,\,r_1,\,r)=\frac{k_d}{2n+1}\left[-r\left(\frac{r}{r_1}\right)^n+r_1\left(\frac{r_1}{r}\right)^n\right] \tag{47}$$

$$\lim_{|k_o r_1|\to 0} D_7(n,\,r_1,\,r) = \begin{cases} -1-k_d^2 r_1 r, & n=0 \\ -\dfrac{n+1}{2n+1}\left(\dfrac{r}{r_1}\right)^n-\dfrac{n}{2n+1}\left(\dfrac{r_1}{r}\right)^{n+1}, & n\neq 0 \end{cases} \tag{48}$$

$$\lim_{|k_o r_2|\to 0}\frac{\hat{H}_n^{(2)}(k_o r_2)}{\hat{H}_n^{(2)'}(k_o r_2)}=\begin{cases} j, & n=0 \\ -\dfrac{k_o r_2}{n}, & n\neq 0 \end{cases} \tag{49}$$

It should be noted that the analytical limits of the combinations (45)–(48) can be evaluated for arguments much smaller than the Schelkunoff Bessel functions individually. This is due to the opposite behaviour of the functions $\hat{J}_n(z)$ and $\hat{N}_n(z)$ for arguments close to zero. The maximum magnitude of the argument $|z_1|$ for which the limits above should be used depends on n. For small values of n this threshold is very small, but as n increases it reaches much larger values. We assumed that $|z_1|$ is the argument for which $\hat{J}_n(.)$ (41) reaches $10^{-\text{Exp1}}$, where Exp1 depends on the precision used. Considering the limits (41)–(44) a simple expression for the threshold can be given by:

$$|z_1|=\begin{cases} 10^{-\text{Exp1}} & n=0 \\ 10^{(1/n+1)[\log_{10}((n+1/2)!/\sqrt{\pi})-\text{Exp1}]} & n\neq 0 \end{cases} \tag{50}$$

(ii) For very large arguments asymptotic expressions of Schelkunoff Bessel functions are used for computing the combinations. From [29]

$$\lim_{|z|\to\infty}\hat{J}_n(z)=\cos(z-(n+1)\pi/2) \tag{51}$$

$$\lim_{|z|\to\infty}\hat{N}_n(z)=\sin(z-(n+1)\pi/2) \tag{52}$$

Substituting into (7)–(10):

$$\lim_{|k_o r|\to\infty} D_1(n,\,r_1,\,r)=-\sin[k_d(r-r_1)] \tag{53}$$

$$\lim_{|k_o r|\to\infty} D_3(n,\,r_1,\,r)=\cos[k_d(r-r_1)] \tag{54}$$

$$\lim_{|k_o r|\to\infty} D_5(n,\,r_1,\,r)=-\sin[k_d(r-r_1)] \tag{55}$$

$$\lim_{|k_o r|\to\infty} D_7(n,\,r_1,\,r)=-\cos[k_d(r-r_1)] \tag{56}$$

$$\lim_{|k_o r_2|\to\infty}\frac{\hat{H}_n^{(2)}(k_o r_2)}{\hat{H}_n^{(2)'}(k_o r_2)}=j \tag{57}$$

The use of these asymptotic limits are especially important for the case when the imaginary part of the arguments of the Schelkunoff Bessel functions are large and present an exponential behaviour. In this case asymptotic limits (53)–(56) also present an exponentially behaviour, but regarding to the difference of the arguments, allowing the combinations of Schelkunoff Bessel functions to be calculated much further. The minimum value of the magnitude of the argument ($|z_2|$) from which the asymptotic limits are used is specified depending on the precision used.

(iii) If the magnitude of the argument of the Bessel functions lies between $|z_1|$ and $|z_2|$ the numerical routines can be used without numerical problems.

The MoM with the aid of the numerical procedure presented allows the analysis to be performed on electrically large problems, where differential methods, or those which uses volume discretisation, may face computational limitations.

4 Input and mutual impedances

For a single patch ($N_p=1$) the input impedance is given by the variational expression [29]

$$Z_{\text{in}}=-\frac{1}{I_o^2}\int\int_S \bar{E}(\bar{J}_s)\cdot\bar{J}_{f1}\,ds \tag{58}$$

where $\bar{J}_s$ represents the total surface current distribution on the patch, including θ and ϕ components. Expanding the currents in basis

IET Microw. Antennas Propag., 2016, Vol. 10, Iss. 1, pp. 53–60

functions, and using (39) together with reciprocity theorem, results

$$Z_{\text{in}} = \frac{1}{I_{\text{o}}^2}\left[\sum_{q}^{Q_\theta}\sum_{p}^{P_\theta} a_{1qp} V_{1qp}^{\theta} + \sum_{q}^{Q_\phi}\sum_{p}^{P_\phi} b_{1qp} V_{1qp}^{\phi}\right] \tag{59}$$

where the initial values of q and p depend on the set of basis functions used.

Now consider the presence of 2 patches ($N_p = 2$), but only the first patch is fed through a coaxial cable. The currents on both patches are determined from MoM, with coefficients a_{iqp} and b_{iqp}, with the elements of the voltage vector denoted as $\boldsymbol{V}_{iqp}^{1\theta}$ and $\boldsymbol{V}_{iqp}^{1\phi}$, where the superscript 1 emphasises that only patch 1 is fed. The self and mutual impedances are given by [29]

$$Z_{11} = -\frac{1}{I_{\text{o}}^2(1)}\iint_S \bar{E}(\bar{J}_{\text{s}})\cdot\bar{J}_{f1}\,\text{d}s \tag{60}$$

$$Z_{21} = -\frac{1}{I_{\text{o}}(1)I_{\text{o}}(2)}\iint_S \bar{E}(\bar{J}_{\text{s}})\cdot\bar{J}_{f2}\,\text{d}s \tag{61}$$

where $\bar{J}_{\text{s}}$ represents the surface current distribution on both patches. Similarly to (59) the self-impedance can be shown as

$$Z_{11} = \frac{1}{I_{\text{o}}^2(1)}\sum_{i=1}^{2}\left[\sum_{q=1}^{Q_\theta}\sum_{p=0}^{P_\theta} a_{iqp}\boldsymbol{V}_{iqp}^{1\theta} + \sum_{q=0}^{Q_\phi}\sum_{p=1}^{P_\phi} b_{iqp}\boldsymbol{V}_{iqp}^{1\phi}\right] \tag{62}$$

The mutual impedance can be written as

$$Z_{21} = \frac{1}{I_{\text{o}}(1)I_{\text{o}}(2)}\sum_{i=1}^{2}\left[\sum_{q=1}^{Q_\theta}\sum_{p=0}^{P_\theta} a_{iqp}\boldsymbol{V}_{iqp}^{2\theta} + \sum_{q=0}^{Q_\phi}\sum_{p=1}^{P_\phi} b_{iqp}\boldsymbol{V}_{iqp}^{2\phi}\right] \tag{63}$$

where $\boldsymbol{V}_{iqp}^{2\theta}$ and $\boldsymbol{V}_{iqp}^{2\phi}$ are the elements of the voltage vector as if only the patch 2 was fed.

5 Arrays of quasi-trapezoidal patches

Consider the situation where there are two or more quasi-trapezoidal patches ($N_p \geq 2$), forming an array, as shown in the top view in Fig. 3 for four patches. As it can be observed the quasi-trapezoidal shape naturally adjusts to the spherical geometry. The input impedance at any of the patches, for example patch n, can be obtained from

$$Z_n = -\frac{1}{I_{\text{o}}(n)^2}\iint_S \bar{E}(\bar{J}_{\text{s}})\cdot\bar{J}_{fn}\,\text{d}s \tag{64}$$

where $\bar{J}_{\text{s}}$ represents the surface current distribution on all N_p patches, fed by currents $I_{\text{o}}(i)$, $i = 1, \ldots, N_p$, and $\bar{J}_{fn}$ is the current distribution at feed n. Using the basis functions expansions (20) and (21), and reciprocity theorem, Z_n can be written as

$$Z_n = \frac{1}{I_{\text{o}}(n)^2}\sum_{i=1}^{N_p}\left[\sum_{q=1}^{Q_\theta}\sum_{p=0}^{P_\theta} a_{iqp}V_{iqp}^{\theta n} + \sum_{q=0}^{Q_\phi}\sum_{p=1}^{P_\phi} b_{iqp}V_{iqp}^{\phi n}\right] \tag{65}$$

where $V_{iqp}^{\theta n}$ and $V_{iqp}^{\phi n}$ are elements of the voltage matrix $\boldsymbol{V}$ (39) for the case when only the feed n is exciting the array, that is, $J_f(r, \theta, \phi) = J_{fn}(r, \theta, \phi)$.

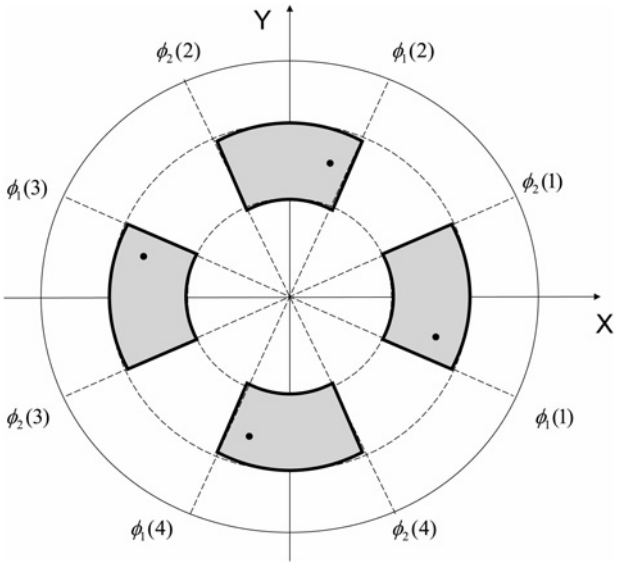

Fig. 3 *Top view of symmetric array of quasi-trapezoidal patches, with 4 elements*

6 Results

For validation of the formulation consider initially that only one quasi-trapezoidal patch is present, centred at $\theta_{\text{c}} = 90^\circ$. In this case the shape of the patch reduces to a quasi-rectangular one, and the results can be compared with previous theoretical ones and measurements. The metallic sphere has radius $r_1 = 18.5$ cm, covered by a foam of thickness $h = 4.5$ mm and dielectric constant $\varepsilon_r = 1$. The patch has width $W_\theta = 20$ cm in θ-direction, an mean width $W_\phi = 20$ cm cm in ϕ-direction, and is centred at $\phi_{\text{c}} = 0^\circ$. The patch is ϕ-polarised with the feed point $d_\phi = 8$ cm from the patch centre, and modelled as a strip of width $W_f = 6.5$ mm. Fig. 4 shows the results for input impedance obtained from this formulation, and compares them with theoretical and measurements from [19]. There is an excellent agreement, and it is observed a frequency shift from the measurements of 3.2 MHz at resonance.

The effect of the quasi-trapezoidal shape on the input impedance can be observed in Fig. 5 which shows the cases where the patch is centred at $\theta_{\text{c}} = 55^\circ$ and at $\theta_{\text{c}} = 45^\circ$, and compares them with the quasi-rectangular case ($\theta_{\text{c}} = 90^\circ$). To allow a fair comparison, the width W_θ and the mean width W_ϕ of the patches were kept the same for all cases, although it should be observed that the shapes of the patches are different as its position is varied. As can be observed from Fig. 5 there is a shift of the resonant frequency and a bandwidth increase, as the patch is moved upwards (smaller θ_{c}). As it happens the difference of width in ϕ-direction on the top and bottom of the patch ($\theta = \theta_1$ and $\theta = \theta_2$) increases, affecting the input impedance.

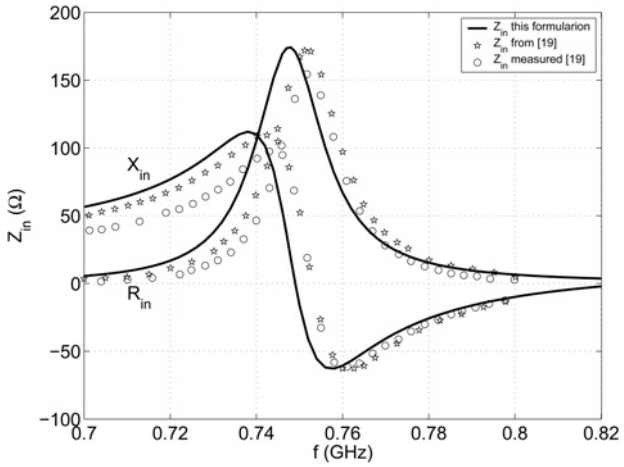

Fig. 4 *Input impedance of 1 quasi-rectangular patch (quasi-trapezoidal centred at $\theta_c = 90^\circ$). $r_1 = 18.5$ cm, $h = 4.5$ mm, $\varepsilon_r = 1$, $W_\theta = W_\phi = 20$ cm, $\phi_c = 0^\circ$, $d_\theta = 0$, $d_\phi = 8$ cm, and $W_f = 6.5$ mm*

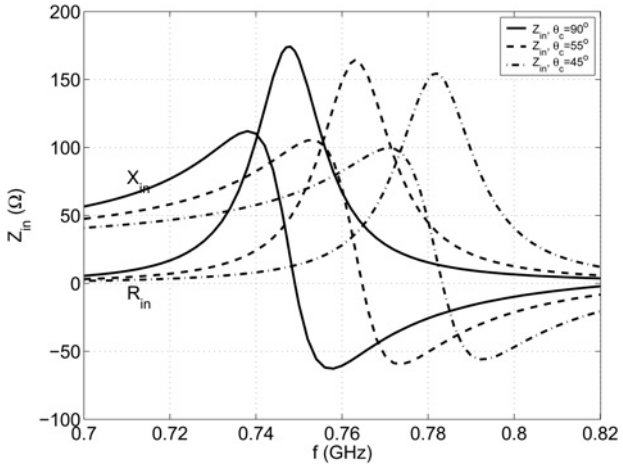

Fig. 5 *Input impedance of 1 patch, for $\theta_c = 45^\circ$, $\theta_c = 55^\circ$, and $\theta_c = 90^\circ$. $r_1 = 18.5$ cm, $h = 4.5$ mm, $\varepsilon_r = 1$, $W_\theta = W_\phi = 20$ cm, $\phi_c = 0^\circ$, $d_\theta = 0$, $d_\phi = 8$ cm, and $W_f = 6.5$ mm*

Results for Z_{11} and for the mutual impedance Z_{12} between two patches whose centres are separated by $d_{12} = 30$ cm are shown in Figs. 6 and 7. The dimensions of each patch is the same as shown in Fig. 5. Results are shown for quasi-rectangular patches ($\theta_c = 90^\circ$) and for quasi-trapezoidal ones, centred at $\theta_c = 45^\circ$ and $\theta_c = 55^\circ$. Comparing the results from Figs. 5 and 6 it can be seen that Z_{11} values are close to the input impedance of a single patch. That both Z_{11} and Z_{12} present frequency shift when the patches moves towards the z-axis. Fig. 8 shows the mutual coupling coefficient for the same two patches 30 cm apart considering $Z_o = 50\ \Omega$. As expected the maximum coupling also presents a frequency shift as the patches move upwards.

Consider a 4-element array equally spaced ($\phi_c(1) = 0^\circ$, $\phi_c(2) = 90^\circ$, $\phi_c(3) = 180^\circ$, and $\phi_c(4) = 270^\circ$), as shown in Fig. 3, and centred at either $\theta_c = 90^\circ$, $\theta_c = 45^\circ$, or $\theta_c = 30^\circ$. When $\theta_c = 90^\circ$ the patches are quasi-rectangular, while for $\theta_c = 45^\circ$ or $\theta_c = 30^\circ$ the patches are quasi-trapezoidal. The patches are kept the same $W_\theta = W_\phi = 10$ cm for all cases. Initially all patches are symmetrically excited, with feed currents of the same magnitude and phase. For each case the radiation pattern was evaluated close to the resonant frequency, that is, at $f = 1.40$ GHz for $\theta_c = 90^\circ$, at $f = 1.42$ GHz for $\theta_c = 45^\circ$, and at $f = 1.435$ GHz for $\theta_c = 30^\circ$.

Fig. 9 shows the radiation pattern as a function of θ, for $\phi = 0$. It is observed that as the patches move upwards the maximum radiation approaches the z-axis, but due to the symmetry of excitation there

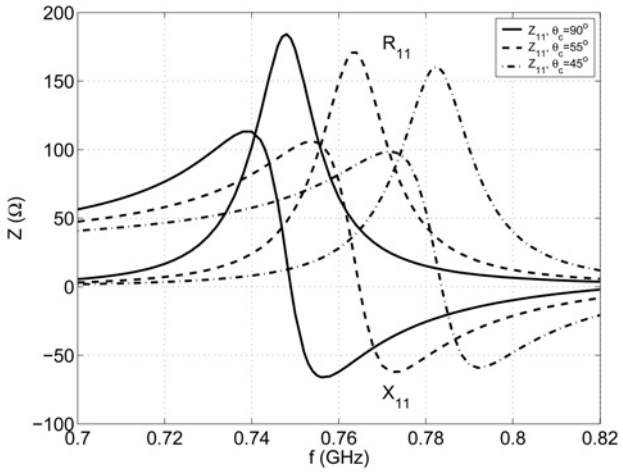

Fig. 6 *Z_{11} for $\theta_c = 45^\circ$, $\theta_c = 55^\circ$ and $\theta_c = 90^\circ$. $r_1 = 18.5$ cm, $h = 4.5$ mm, $\varepsilon_r = 1$, $W_\theta = W_\phi = 20$ cm, $\phi_c(1) = 0^\circ$, $d_{12} = 30$ cm, $d_\theta = 0$, $d_\phi = 8$ cm, and $W_f = 6.5$ mm*

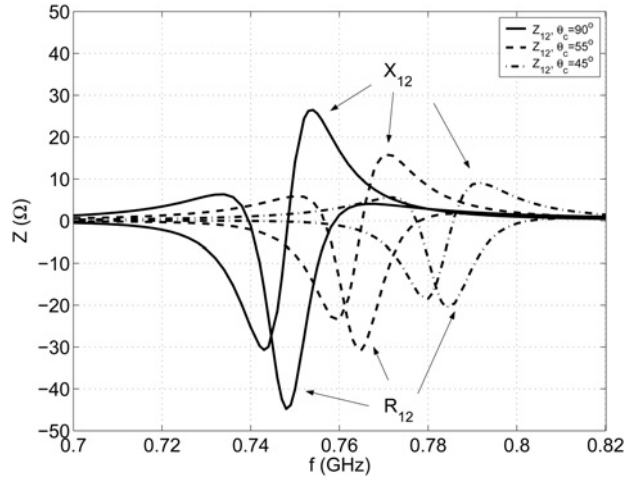

Fig. 7 *Z_{12} for $\theta_c = 45^\circ$, $\theta_c = 55^\circ$ and $\theta_c = 90^\circ$. $r_1 = 18.5$ cm, $h = 4.5$ mm, $\varepsilon_r = 1$, $W_\theta = W_\phi = 20$ cm, $\phi_c(1) = 0^\circ$, $d_{12} = 30$ cm, $d_\theta = 0$, $d_\phi = 8$ cm, and $W_f = 6.5$ mm*

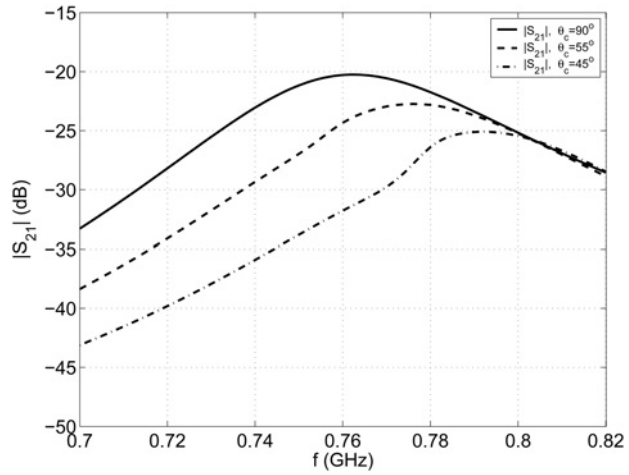

Fig. 8 *S_{21} for $\theta_c = 45^\circ$, $\theta_c = 55^\circ$ and $\theta_c = 90^\circ$. $r_1 = 18.5$ cm, $h = 4.5$ mm, $\varepsilon_r = 1$, $W_\theta = W_\phi = 20$ cm, $\phi_c(1) = 0^\circ$, $d_{12} = 30$ cm, $d_\theta = 0$, $d_\phi = 8$ cm, and $W_f = 6.5$ mm*

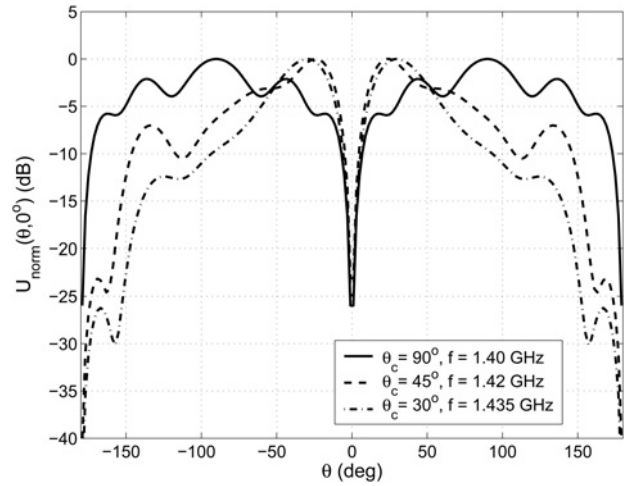

Fig. 9 *Radiation patterns of symmetrical 4-element arrays of quasi-trapezoidal patches, $\phi = 0^\circ$, and $\theta_c = 90^\circ$, 45°, and 30°. $r_1 = 18.5$ cm, $h = 3.8$ mm, $\varepsilon_r = 1$, $W_\theta = W_\phi = 10$ cm, $\phi_c(1) = 0^\circ$, $\phi_c(2) = 90^\circ$, $\phi_c(3) = 180^\circ$, and $\phi_c(4) = 270^\circ$, $d_\theta = 0$, $d_\phi = 4$ cm, $I_o(i) = 1$ mA, $i = 1, \ldots, 4$, and $W_f = 6.5$ mm*

IET Microw. Antennas Propag., 2016, Vol. 10, Iss. 1, pp. 53–60

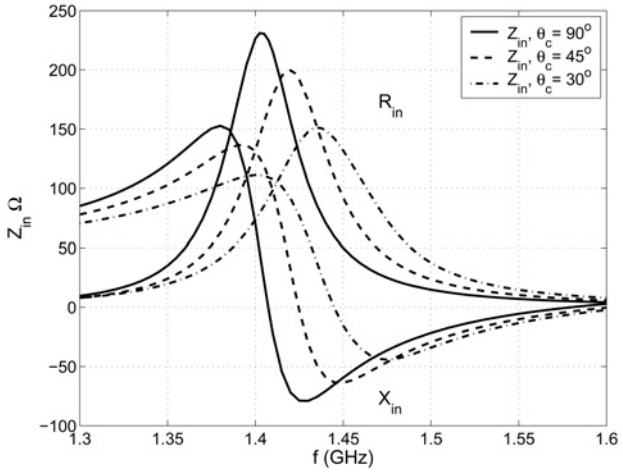

Fig. 10 *Input impedance at each patch of symmetrical 4-element arrays of quasi-trapezoidal patches centred at $\theta_c = 90^\circ$, 45°, and 30°. $r_1 = 18.5$ cm, $h = 3.8$ mm, $\varepsilon_r = 1$, $W_\theta = W_\phi = 10$ cm, $\phi_c(1) = 0^\circ$, $\phi_c(2) = 90^\circ$, $\phi_c(3) = 180^\circ$, and $\phi_c(4) = 270^\circ$, $d_\theta = 0$, $d_\phi = 4$ cm, $I_o(i) = 1$ mA, $i = 1, \ldots, 4$, and $W_f = 6.5$ mm*

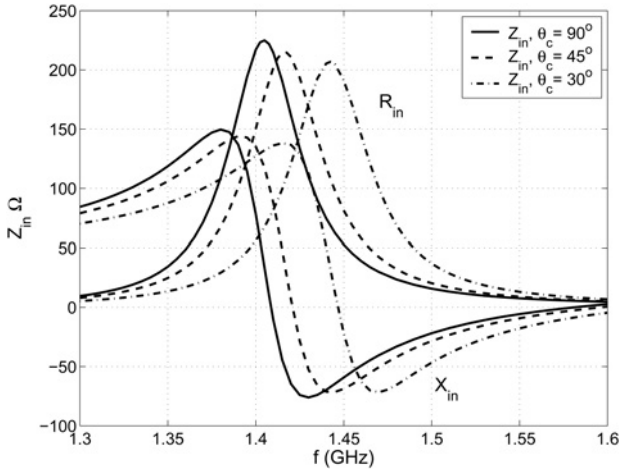

Fig. 12 *Input impedance at each patch of asymmetrical 4-element arrays of quasi-trapezoidal patches centred at $\theta_c = 90^\circ$, 45°, and 30°. $r_1 = 18.5$ cm, $h = 3.8$ mm, $\varepsilon_r = 1$, $W_\theta = W_\phi = 10$ cm, $\phi_c(1) = 0^\circ$, $\phi_c(2) = 90^\circ$, $\phi_c(3) = 180^\circ$, and $\phi_c(4) = 270^\circ$, $d_\theta = 0$, $d_\phi = 4$ cm, $I_o(1) = I_o(2) = 1$ mA, $I_o(3) = I_o(4) = -1$ mA, and $W_f = 6.5$ mm*

is a null at $\theta = 0^\circ$. The input impedance at each patch is shown in Fig. 10. As each element of the array is excited at the same position regarding the patch, and the feed currents have the same magnitude and phase, the input impedances of all the array elements are equal. Fig. 10 shows that the radiation resistance of quasi-trapezoidal arrays of patches that have the same mean widths depend on the central value θ_c. For smaller values of θ_c the resonance shifts in frequency, and the maximum input resistance is reduced, while the bandwidth increases. These effects are due to the different shapes of the patches for different values of central angle θ_c, as well as to the coupling among the elements.

To avoid the null in the z-axis the same arrays presented in Figs. 9 and 10 are now asymmetrically excited. The magnitude of the feed currents are the same, two of the elements are excited in-phase ($I_o(1) = I_o(2) = 1$ mA), and the remaining ones are excited out-of-phase ($I_o(3) = I_o(4) =$ -1 mA). In this case while the patches are moved to smaller values of θ_c, the directions of maximum radiation move to the z-axis, as shown in Fig. 11. The input impedances of the elements of this array are also equal and presented at Fig. 12. It is again observed an increase in bandwidth and frequency shift of the resonant frequency as θ_c diminishes.

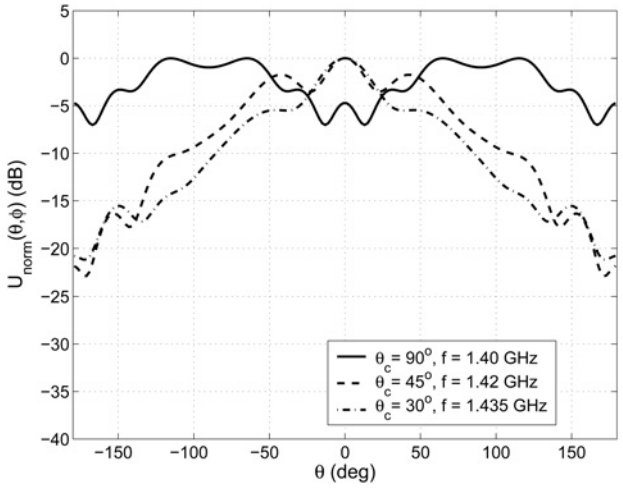

Fig. 11 *Radiation patterns of asymmetrical 4-element arrays of quasi-trapezoidal patches, $\phi = 0^\circ$, and $\theta_c = 90^\circ$, 45°, and 30°. $r_1 = 18.5$ cm, $h = 3.8$ mm, $\varepsilon_r = 1$, $W_\theta = W_\phi = 10$ cm, $\phi_c(1) = 0^\circ$, $\phi_c(2) = 90^\circ$, $\phi_c(3) = 180^\circ$, and $\phi_c(4) = 270^\circ$, $d_\theta = 0$, $d_\phi = 4$ cm, $I_o(1) = I_o(2) = 1$ mA, $I_o(3) = I_o(4) = -1$ mA, and $W_f = 6.5$ mm*

Comparing the results for symmetrical arrays in Fig. 10 to those for asymmetrical arrays in Fig. 12 we can observe little difference when the patches are centred at $\theta_c = 90^\circ$, but significant ones for $\theta_c = 45^\circ$ and $\theta_c = 30^\circ$. It can be understood as θ_c diminishes the elements of the arrays are closer to each other, which increases the coupling effect on the input impedance.

7 Conclusions

This paper presented a method of moment analysis of quasi-trapezoidal spherical patches using full-domain basis functions. A procedure was presented that avoids numerical problems for evaluating combinations of Schelkunoff Bessel Functions on the MoM matrix elements. The analysis included the input impedance of a single patch, mutual impedance, radiation pattern and input impedance of an array element. A frequency shift of resonance and bandwidth increase were observed when the shape of the patch moves away from the quasi-rectangular, toward a quasi-trapezoidal one, that is, as the patch is moved closer to the z-axis.

8 Acknowledgment

This work was partially supported by FACEPE and CNPq.

9 References

1 Wong, K.-L.: 'Design of nonplanar microstrip antennas and transmission lines' (John Wiley & Sons, 1999)
2 Garg, R., Bhartia, P., Bahl, I., *et al.*: 'Microstrip antenna design handbook' (Artech House, 2001)
3 Josefsson, L., Persson, P.: 'Conformal array antenna theory and design' (Wiley-Interscience, New Jersey, 2006)
4 Krowne, C.M.: 'Radiation efficiency for spherical-rectangular microstrip antenna'. Proc. AP-S International Symposium, 1982, vol. 20, pp. 171–174
5 Wu, K.Y., Kauffman, J.F.: 'Radiation pattern for spherical-rectangular microstrip antennas'. IEEE Antennas Propagation Int. Symp. Digest, 1983, pp. 43–46
6 Tam, W.Y., Luk, K.M.: 'Patch antennas on a spherical body', *IEE Proc.-H.*, 1991, **138**, (1), pp. 103–108
7 Das, A., Das, S.K., Narasimhan, M.S.: 'Radiation characteristics of wraparound microstrip antenna on spherical body', *IEEE Trans. Antennas Propag.*, 1991, **39**, pp. 1031–1034
8 Descardeci, J.R., Lima, A.C.C., Giarola, A.J.: 'Microstrip antenna on a spherical surface', *IEEE AP-S Digest*, 1991, **2**, pp. 820–823
9 Ferreira, D.B., Lacava, J.C. da S.: 'Microstrip antennas conformed onto spherical surfaces', in Nasimuddin, N. (Ed.): 'Microstrip antennas' (Intech, 2011, 1st edn.), pp. 83–108

10 Tam, W.Y., Luk, K.M.: 'Far field analysis of spherical-circular microstrip antennas by electric surface current models', *IEE Proc.-H.*, 1991, **138**, (1), pp. 98–102
11 Ke, B., Kishk, A.A.: 'Analysis of spherical circular microstrip Antennas', *IEE Proc.-H.*, 1991, **138**, (6), pp. 542–548
12 Kishk, A.A.: 'Analysis of spherical annular microstrip antennas', *IEEE Trans. Antennas Propag.*, 1993, **41**, (3), pp. 338–343
13 Tam, W.-Y., Luk, K.-M.: 'Resonance in spherical-circular microstrip structures', *IEEE Trans. Microw. Theory Tech.*, 1991, **39**, (4), pp. 700–704
14 Wong, K.-L., Hsiao, S.-F., Chen, H.-T.: 'Resonance and radiation of a superstrateloaded spherical-circular microstrip patch antenna', *IEEE Trans. Antennas Propag.*, 1993, **41**, (5), pp. 686–690
15 Tam, W.Y., Lai, A.K.Y., Luk, K.M.: 'Input Impedance of spherical microstrip antenna', *IEE Proc. Microw. Antennas Propag.*, 1995, **142**, (3), pp. 285–288
16 Sipus, Z., Burum, N., Bartolic, J.: 'Analysis of rectangular microstrip patch antennas on spherical structures', *Microw. Opt. Technol. Lett.*, 2003, **36**, (4), pp. 276–280
17 Burum, N., Sipus, Z., Bartolic, J.: 'Mutual coupling between spherical-rectangular microstrip antennas', *Microw. Opt. Technol. Lett.*, 2004, **40**, (5), pp. 387–391
18 Giang, T.V.B.: 'A systematic approach to the analysis of spherical multilayer structures and its applications'. PhD Thesis, Technical University of Hamburg-Harburg, 2005
19 Sipus, Z., Burum, N., Skokic, S., *et al.*: 'Analysis of spherical arrays of microstrip antennas using moment method in spectral domain', *IEE Proc. Microw. Antennas Propag.*, 2006, **153**, (6), pp. 533–543
20 Costa, L.A., Pereira-Filho, O.M.C., Moreira, F.J.S.: 'Input impedance of rectangular microstrip antennas on spherical bodies using MoM and attachment modes', *IEEE AP-S Digest*, 2006, **1**, pp. 3947–3950
21 Sipus, Z., Kildal, P.-S., Leijon, R., *et al.*: 'An algorithm for calculating green's functions for planar, circular cylindrical and spherical multilayer substrates', *Appl. Comput. Electromagn. Soc. J.*, 1998, **13**, pp. 243–254
22 Okhmatovski, V.I., Cangellaris, A.C.: 'Efficient calculation of the electromagnetic dyadic green's function in spherical layered media', *IEEE Trans. Antennas Propag.*, 2003, **51**, (12), pp. 3209–3220
23 Giang, T.V.B., Dreher, A.: 'Analysis method of microstrip antennas on hemispherical multilayer structures', *IEEE Trans. Antennas Propag.*, 2008, **56**, (10), pp. 3324–3327
24 Khamas, S.K.: 'A generalized asymptotic extraction solution for antennas in multilayered spherical media', *IEEE Trans. Antennas Propag.*, 2010, **58**, (11), pp. 3343–3347
25 Tsitsas, N.L., Valagiannopoulos, C.A.: 'Mathematical modeling of spherical microstrip antennas and applications', in Nasimuddin, N. (Ed.): 'Microstrip antennas' (Intech, 2011, 1st edn.), pp. 109–130
26 Khamas, S.K.: 'Electromagnetic radiation by antennas of arbitrary shape in a layered spherical media', *IEEE Trans. Antennas Propag.*, 2009, **57**, (12), pp. 3827–3834
27 Meiguni, J.S., Kamyab, M., Hosseinbeig, A.: 'Theory and experiment of spherical aperture-coupled antennas', *IEEE Trans. Antennas Propag.*, 2013, **61**, (5), pp. 2397–2403
28 Harrington, R.F.: 'Field computation by moment method' (Macmillian, New York, 1968)
29 Harrington, R.F.: 'Time-harmonic electromagnetic fields' (McGraw-Hill, New York, 1961)
30 Richards, W.F., Lo, Y.T., Harrison, D.D.: 'An improved theory for microstrip antennas and applications', *IEEE Trans. Antennas Propag.*, 1981, **29**, (1), pp. 38–46

10 Appendix: Normalised vector Legendre series

A two-dimensional field $\bar{J}(\theta, \phi)$ can be written in a normalised vector Legendre series [10, 16] as:

$$\begin{aligned}\bar{J}(\theta, \phi) &= \begin{bmatrix} J_\theta(\theta, \phi) \\ J_\phi(\theta, \phi) \end{bmatrix} \\ &= \sum_{m=-\infty}^{\infty} \sum_{n=|m|}^{\infty} \frac{1}{\sqrt{S(n)}} \bar{\bar{L}}(n, m, \theta) \tilde{J}(n, m)\, \mathrm{e}^{\mathrm{j}m\phi}\end{aligned} \tag{66}$$

where

$$\begin{aligned}\tilde{J}(n, m) &= \begin{bmatrix} J_u(n, m) \\ J_d(n, m) \end{bmatrix} \\ &= \frac{1}{\sqrt{S(n)}} \int_0^{\pi} \int_{-\pi}^{\pi} \bar{\bar{L}}(n, m, \theta) \bar{J}(\theta, \phi)\, \mathrm{e}^{-\mathrm{j}m\phi} \sin\theta \, \mathrm{d}\theta \, \mathrm{d}\phi\end{aligned} \tag{67}$$

$$\bar{\bar{L}}(n, m, \theta) = \begin{bmatrix} \dfrac{\partial}{\partial\theta} \bar{P}_n^{|m|}(\cos\theta) & -\mathrm{j}m \dfrac{\bar{P}_n^{|m|}(\cos\theta)}{\sin\theta} \\ \mathrm{j}m \dfrac{\bar{P}_n^{|m|}(\cos\theta)}{\sin\theta} & \dfrac{\partial}{\partial\theta} \bar{P}_n^{|m|}(\cos\theta) \end{bmatrix} \tag{68}$$

$$S(n) = 4\pi \frac{n(n+1)}{2n+1} \tag{69}$$

and the normalised associated Legendre functions $\bar{P}_n^m(.)$ relates to the associated Legendre functions $P_n^m(.)$ by:

$$\bar{P}_n^m(\cos\theta) = \sqrt{\frac{(n-m)!}{(n+m)!}} P_n^m(\cos\theta) \tag{70}$$